

A High-Performance Alloy-Based Anode Enabled by Surface and Interface Engineering for Wide-Temperature Sodium-Ion Batteries

Jian Yang, Xin Guo,* Hong Gao, Tianyi Wang,* Zhigang Liu, Qing Yang, Hang Yao, Jiabao Li, Chengyin Wang, and Guoxiu Wang*

Alloy-based anodes have shown great potential to be applied in sodium-ion batteries (SIBs) due to their high theoretical capacities, suitable working potential, and abundant earth reserves. However, their practical applications are severely impeded by large volume expansion, unstable solid-electrolyte interfaces (SEI), and sluggish reaction kinetics during cycling. Herein, a surface engineering of tin nanorods via N-doped carbon layers (Sn@NC) and an interface engineering strategy to improve the electrochemical performance in SIBs are reported. In particular, the authors demonstrate that uniform surface modification can effectively facilitate electron and sodium transport kinetics, confine alloy pulverization, and simultaneously synergize interactions with the ether-based electrolyte to form a robust organic-inorganic SEI. Moreover, it is discovered that the diethylene glycol dimethyl ether electrolyte with strong stability and an optimized Na⁺ solvation structure can co-embed the carbon layer to achieve fast reaction kinetics. Consequently, Sn@NC anodes deliver extra-long cycling stability of more than 10 000 cycles. The full cell of Na₃V₂(PO₄)₃ || Sn@NC exhibits high energy density (215 Wh kg⁻¹), excellent high-rate capability (reaches 80% capacity in 2 min), and long cycle life over a wide temperature range of -20 to 50 °C.

been successfully developed for SIBs.^[2-5] Whereas, the development of safe, low-cost, and high-performance anode materials still faces critical challenges owing to the large radius of Na⁺ ions, sluggish sodium intercalation reaction kinetics, and poor stability.^[6-8] Hard carbon with the typical intercalation/absorption reaction mechanism during the electrochemical process has been used as anode materials for SIBs. However, its limited specific capacity (≈300 mAh g⁻¹) can not meet the growing requirement of high energy density devices, and the low sodiation potential probably causes the pernicious Na metal deposition, leading to safety concerns.^[9-12]

In order to increase the competitiveness of SIBs, alloy-type anode materials with high theoretical capacities have drawn extensive attention. Generally, those elements with earth-abundant reserves, safe sodiation potentials, and environmental friendliness are especially beneficial for large-scale energy


storage.^[12-15] Metallic tin, as a typical alloy-type anode material, delivers a high theoretical specific capacity of 847 mAh g⁻¹ after being sodiated to form Na₁₅Sn₄. Coupled with its low cost and environmental benignity, Sn is regarded as a prospective anode material for SIBs. However, 420% of volume expansion and

1. Introduction

In recent years, sodium-ion batteries (SIBs) have emerged as promising low-cost rechargeable battery systems for renewable energy storage.^[1] Various appropriate cathode materials have

J. Yang, T. Wang, Z. Liu, Q. Yang, H. Yao, J. Li, C. Wang
Institute for Innovative Materials and Energy
Faculty of Chemistry and Chemical Engineering
Yangzhou University
Yangzhou 225002, China
E-mail: wangty@yzu.edu.cn

J. Yang
Key Lab of Fluorine and Silicon for Energy Materials and Chemistry of
Ministry of Education
College of Chemistry and Chemical Engineering
Jiangxi Normal University
Nanchang 330022, China
X. Guo, H. Gao, G. Wang
Centre for Clean Energy Technology
School of Mathematics and Physics Science
Faculty of Science
University of Technology Sydney
Sydney, NSW 2007, Australia
E-mail: xin.guo@uts.edu.au; guoxiu.wang@uts.edu.au

 The ORCID identification number(s) for the author(s) of this article can be found under <https://doi.org/10.1002/aenm.202300351>

© 2023 The Authors. Advanced Energy Materials published by Wiley-VCH GmbH. This is an open access article under the terms of the Creative Commons Attribution License, which permits use, distribution and reproduction in any medium, provided the original work is properly cited.

DOI: 10.1002/aenm.202300351

continuous damage/re-growth of the solid electrolyte interphase (SEI) during sodiation and desodiation causes pulverization of the active material and even peeling off from the underlying current collector substrates.^[16–18]

Electrode structure engineering is one of the most prevailing and effective strategies to ameliorate the above issues.^[19] Meanwhile, several studies in recent years have revealed that electrolytes can greatly affect the structural evolution and electrochemical performance of alloy-type anodes in SIBs.^[20] This is corroborated by ether-based electrolytes with favorable lower resistance for catering to the requirements of alloy anodes.^[21] For example, electrolytes with NaPF₆ in glymes are demonstrated to be beneficial for forming a stable SEI layer on the surface of Sn- and Bi-based anodes to resist structural distortion during cycling.^[22,23] However, this result is challenged by a recent study that claims that the decomposition of NaPF₆ during the SEI formation may inevitably generate harmful HF that could attack alloy anodes and deteriorate their performance.^[24,25] Therefore, the compatibility between the designed electrodes and organic electrolytes is an essential factor that needs to be considered, because it will directly affect the mass transfer efficiency and SEI chemistry, which determines the rate capability and long-term cycling performance.

A facile pre-surface modification on the active materials would be an effective strategy to suppress the aforementioned side reactions and simultaneously confine the volume change of alloy anodes during sodiation–desodiation. Herein, we rationally designed and synthesized a 3D flower-like architecture consisting of nitrogen-doped carbon-coated tin nanorods (Sn@NC) as anodes for SIBs. Density functional theory (DFT) calculations validate that the surface engineering of tin nanorods by N-doped carbon significantly improves the sodium affinity and sodium ion diffusion kinetics. More importantly, we found that diethylene glycol dimethyl ether (DEGDME)-based electrolyte with remarkable chemical stability and optimized solvation structure could synergistically cooperate with the N-doped carbon layer to produce a stable organic-inorganic hybrid SEI, with an ionic conductive polyether at the outer layer and robust fluorine-rich inorganic compounds at the inner layer. The SEI constitution and the composite structural stability are comprehensively evidenced by a portfolio of ex situ characterization techniques, including in-depth X-ray photoelectron spectroscopy (XPS) analyses, scanning electron microscopy (SEM), and transmission electron microscopy (TEM). Furthermore, theoretical simulations and electrochemical analysis reveal a faster reaction kinetics of Sn@NC anode in the DEGDME-based electrolyte compared to the conventional carbonate electrolyte. Therefore, through the synergy of surface engineering of the N-doped carbon layer and interface engineering by electrolyte modulation, Sn@NC electrodes exhibit a high capacity of 347 mAh g⁻¹ at a high rate of 5 A g⁻¹ even after 10 000 cycles. The Sn@NC||NVP/C full SIBs exhibit no obvious capacity decay over a wide temperature range from –20 °C to 50 °C.

2. Results and Discussion

Figure 1a schematically illustrates the synthesis process of the Sn@NC composite. First, the flower-like SnO₂ nanorods with an average diameter of ≈200 nm were prepared by a hydrothermal

method, and the SnO₂ nanorods were further encapsulated by dopamine (SnO₂@PDA) via an in situ polymerization process (Figures S1 and S2, Supporting Information). Subsequently, the SnO₂@PDA composite was subjected to hydrogen-assisted thermal treatment to obtain Sn@NC flower-like nanorods. During this process, the SnO₂ was reduced to Sn and PDA was decomposed to N-doped carbon simultaneously. The XRD pattern of the resultant Sn@NC composite in Figure 1b exactly matches the tetragonal phase Sn (JCPDS no.04-0673). The SEM images of the Sn@NC present a similar flower-like nanorod architecture as the pristine SnO₂ and SnO₂@PDA, and the corresponding TEM images show a uniform carbon layer coated on the surface of the nanorods (Figure 1c,d). The HRTEM images of Sn@NC reveal that the thickness of the carbon layer is around 13 nm, and the lattice fringes with a 2.06 Å spacing of the inner material can be assigned to the (220) plane of Sn, which is in good agreement with the selected area electron diffraction (SAED) pattern of the composite (Figure 1e,f).^[18] Figure 1g displays the scanning transmission electron microscopy (STEM) image of Sn@NC and the corresponding energy dispersive X-ray (EDX) mapping results. The uniform distribution of Sn in the inner core, and C and N elements on the surface further confirm that metallic Sn is confined in a homogenous N-doped carbon layer.

Raman spectroscopy was employed to investigate the surface structure of as-prepared samples. As shown in Figure S3, Supporting Information, the presence of a D-band at ≈1358 cm⁻¹ and G-band at 1592 cm⁻¹, as well as the disappearance of the characteristics of Sn or SnO₂ indicate the successful surface coating of the dopamine-derived carbon (Figure S3, Supporting Information).^[26,27] Besides this spectroscopy, thermogravimetric analysis (TGA) was used to measure the Sn content in the composite. As the full oxidation of Sn to SnO₂ in air and evaporation of carbon at high temperatures (Figure S4, Supporting information),^[28] it can be deduced that the tin mass ratio is around 83.94 wt% in the Sn@NC composite. The surface chemistries of the synthesized materials were characterized by XPS (Figure S5, Supporting Information). The high-resolution C 1s spectrum of the Sn@NC composite can be deconvoluted into C–C, C–O, C–N, and C=O peaks, respectively (Figure S6, Supporting Information). Compared to the SnO₂@PDA, the C–O peak attenuated and the –NH₂ peaks diminished in the Sn@NC composite, which further verifies that the PDA has been converted to N-doped carbon after heat treatment (Figure S7, Supporting Information).^[29,30] The nitrogen coordination structure in the carbon was revealed by the high-resolution N 1s spectrum, which can be deconvoluted to pyrrolic N, graphitic N, and oxidized N, respectively (Figure 2a).

The effects of surface engineering by N-doped carbon on sodium storage performance were investigated by DFT calculations. The sodium adsorption energies reflect the material's capability for sodium-ion uptake and influence its sodium storage performance. Thus, we calculated the sodium adsorption energies of various carbon and Sn/carbon structures involved in this work (Figure S8, Supporting Information). Figure 2b shows that the N-doped carbons have lower adsorption energies than the pristine carbon, and the Sn@NC exhibits the lowest Na adsorption energy of –4.71 eV, indicating a superior sodium affinity of the surface-engineered composite. Additionally, the sodium diffusion behavior was also studied by simulating three possible

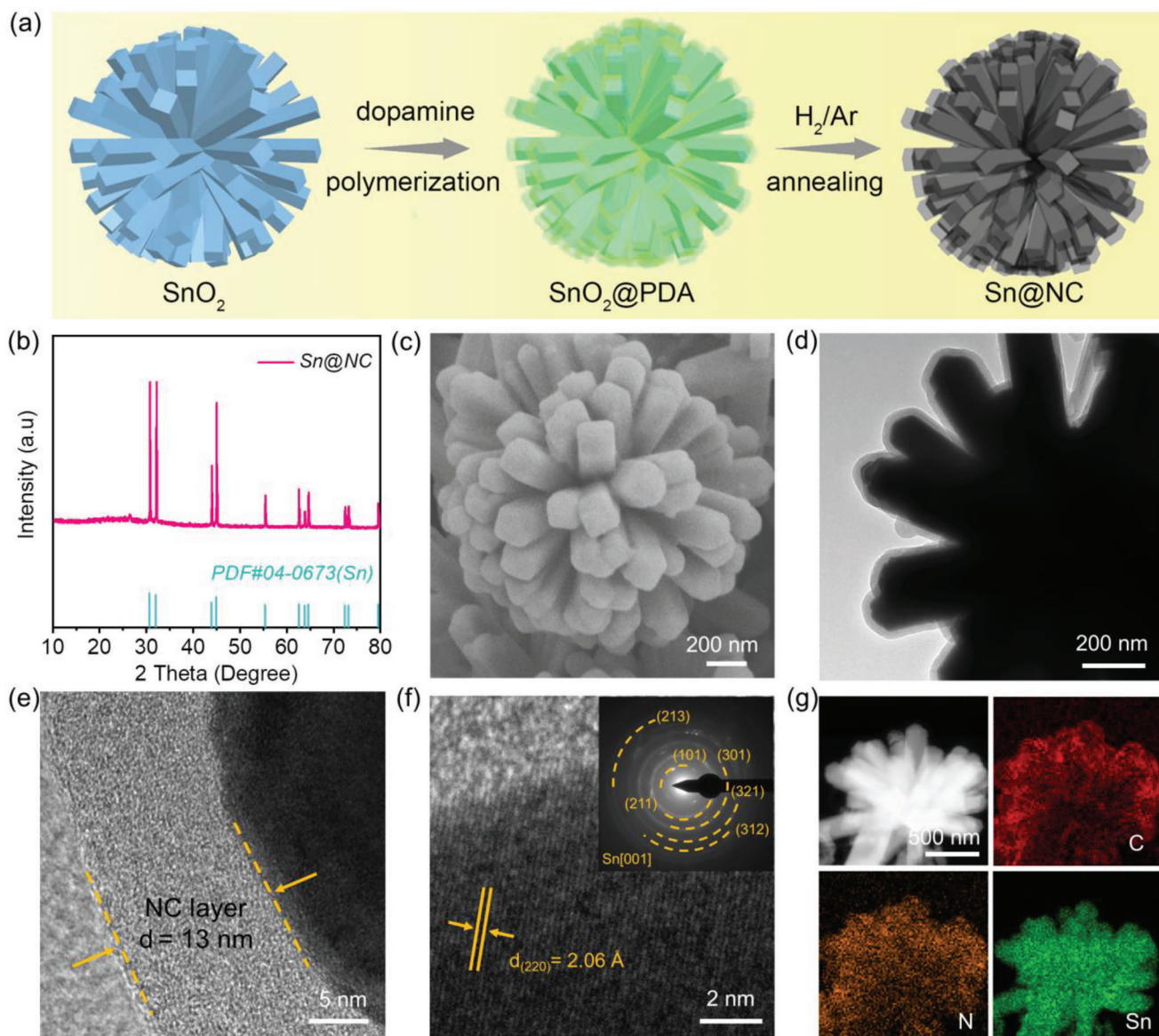


Figure 1. a) Schematic of synthesis of Sn@NC composite. b) XRD pattern, c) SEM, d–f) TEM images, and g) STEM and corresponding EDX mapping images of the Sn@NC composite.

diffusion paths between two adjacent hollow sites of the pristine Sn and Sn@NC (Figure S9, Supporting Information). The sodium diffusion energy barrier on the Sn@NC surface is only around 0.11 eV (Figure 2c). In contrast, the diffusion energy barrier of the same diffusion path on the pristine Sn surface is within the range of 0.30–0.32 eV, demonstrating that the sodium ion diffusion kinetics has been significantly improved after surface engineering.^[30–33]

Although the homogenous N-doped carbon surface is expected to improve the sodium storage performance, the large volume change of the tin during sodiation/desodiation could lead to swelling and shrinking of the electrodes, thereby pulverizing the solid-electrolyte interface (SEI) and deteriorating the cycling performance. Optimizing the Na⁺ solvation structure and constructing a stable SEI can maximize the positive effects of surface en-

gineering and synergistically enhance the electrochemical performance, which could be achieved via the modulation of electrolytes. Therefore, we deliberately examined the sodium storage performance of Sn@NC anodes with a typical carbonate-based electrolyte and a DEGDM-based electrolyte. **Figure 3a,b** shows the galvanostatic discharge/charge curves of the typical Sn@NC anodes at a current density of 0.1 A g⁻¹ in the ethylene carbonate/propylene carbonate (EC/PC)-based electrolyte and DEGDM-based electrolyte, respectively. The Sn@NC composites in both electrolytes display distinct plateaus, corresponding to the typical stepwise alloying and dealloying reactions of metallic tin.^[34–36] We found that the cell with DEGDM-based electrolyte shows much smaller voltage polarization and higher round trip efficiency. Additionally, the use of the DEGDM-based electrolyte improved the initial Coulombic efficiency (CE) of the

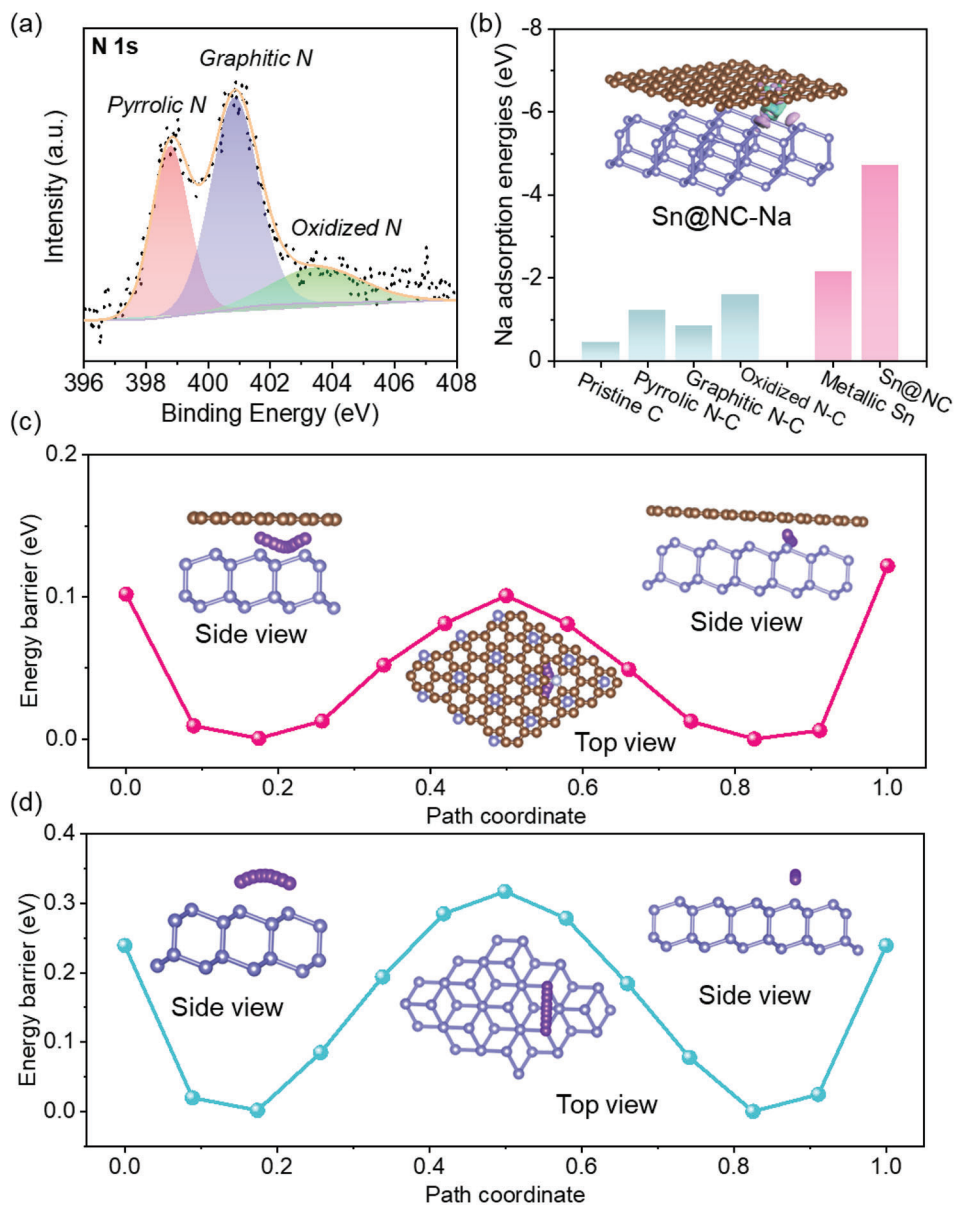


Figure 2. a) High-resolution N 1s XPS of Sn@NC composite. b) The adsorption energies of carbon, pyrrolic N-, graphitic N-, oxidized N-doped carbons, Sn, and Sn@NC for sodium atoms (Inset is the charge difference plot of Sn@NC for sodium atoms). Energy barrier and diffusion path of Na atom diffusion on the surface of c) Sn@NC and d) Sn materials.

cell to 78.4% compared to that using the EC/PC-based electrolyte (62.4%). The remarkably improved initial CE with DEGDM-based electrolyte might be ascribed to the better stability of the DEGDM solvent and SEI formed on the electrodes, which will be further discussed in the next section.

Figure 3c shows the rate capability of Sn@NC in both electrolytes. The Sn@NC electrodes in DEGDM-based electrolyte exhibit a specific capacity of 560, 519, 509, 490, and 437 mAh g⁻¹ at current densities of 0.1, 0.2, 0.5, 1.0, and 5.0 A g⁻¹, respectively. The high specific capacity of 534 mAh g⁻¹ can be restored after the current density is reversed to 0.1 A g⁻¹. Meanwhile, the corresponding voltage gaps between discharge and charge are almost constant as the current increases (Figure S10, Supporting Infor-

mation), indicating the excellent rate capability of the Sn@NC electrodes in DEGDM-based electrolyte. On the contrary, the Sn@NC electrodes in the EC/PC-based electrolyte only deliver a very low capacity of 46 mAh g⁻¹ at a high current of 5.0 A g⁻¹. The dramatic capacity fading at a high current with the EC/PC-based electrolyte could be attributed to the slow reaction kinetics and poor reversibility.^[37,38]

Cyclic voltammetry (CV) curves of typical Sn@NC electrodes at different scan rates in both electrolytes were measured to probe the sodium storage mechanism. The Sn@NC electrodes in DEGDM-based electrolyte show sharp redox peaks, which are consistent with the discharge and charge profiles (Figure 3d). The two reduction peaks (R) of sodiation situated at 0.195 and 0.02 V

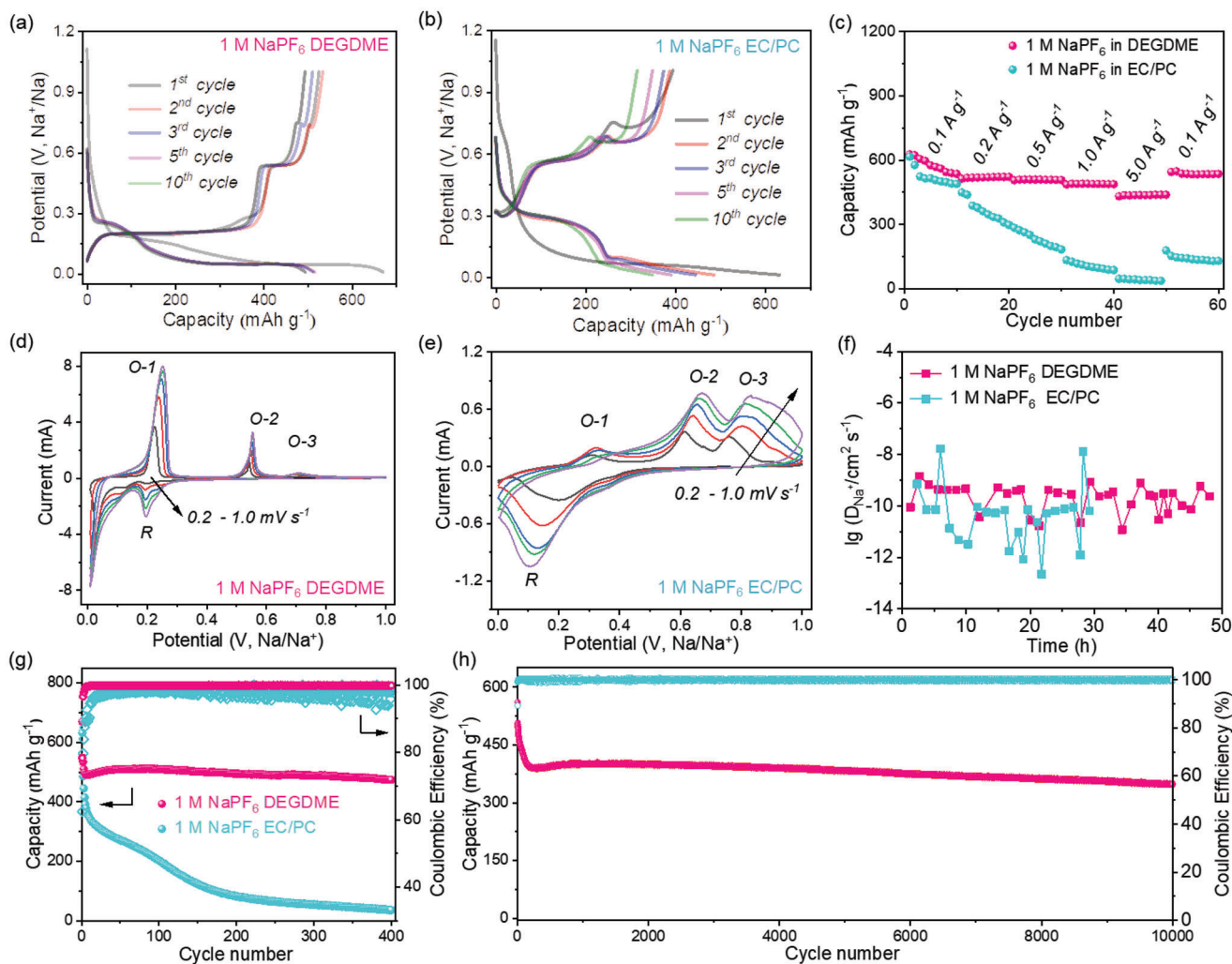


Figure 3. Galvanostatic discharge/charge curves of an Sn@NC anode at 0.1 A g⁻¹ using a) DEGDME- and b) EC/PC-based electrolytes. c) Rate capability of the Sn@NC electrodes with both electrolytes. CV curves of the Sn@NC anode in d) DEGDME- and e) EC/PC-based electrolytes at different scan rates. f) The Na⁺ diffusion coefficient derived from the GITT curves of the cells after 10 cycles. g) Comparison of cycle performance at 1.0 A g⁻¹ in both electrolytes and h) the long cycling performance of composite anodes at 5.0 A g⁻¹ in the DEGDME-based electrolyte.

correspond to the alloying reaction from Sn to Na₁₅Sn₄, and the three oxidation peaks (O-1, O-2, and O-3) can be attributed to the stepwise dealloying process from Na₁₅Sn₄, Na₉Sn₄, and NaSn, to Sn.^[34,35] For the DEGDME-based electrolyte, the predominant anodic peaks are O-1 at 0.22 V and O-2 at 0.54 V, which means that the dealloying process is nearly completed whenever voltages are above these values. When EC/PC-based electrolyte was used, the current response of both reduction and oxidation weakened, and the corresponding redox peaks widened (Figure 3e). Besides these effects, the dominant oxidation peaks become O-2 (0.62 V) and O-3 (0.81 V), which shifted to higher voltage because of the sluggish reaction kinetics within the carbonate electrolyte.^[34–36] The reversible stepwise alloying and dealloying mechanism of the Sn@NC electrodes in the DEGDME-based electrolyte were further verified by ex situ XRD characterizations, which evidence the reaction route of Sn ⇌ NaSn ⇌ Na₉Sn₄ ⇌ Na₁₅Sn₄ upon sodiation and desodiation, respectively (Figure S11, Supporting Information).^[34–36]

The charge storage mechanism analysis reveals that the anodes in both electrolyte systems follow a mixed diffusion-capacitive behavior. However, a higher capacitive contribution has been identified when the DEGDME-based electrolyte was used (Figures S12 and S13, Supporting Information). Meanwhile, by comparing the capacitive contribution of the Sn@NC and blank Sn nanorod electrodes in the DEGDME-based electrolyte, it can be inferred that the NC surface synergistically facilitates the capacitive behavior of the alloy anode (Figures S14 and S15, Supporting Information). The faster kinetic behavior in the DEGDME-based electrolyte is further demonstrated by the galvanostatic intermittent titration technique (GITT). Figure S16, Supporting Information shows the GITT curves of Sn@NC anodes in both electrolytes. It is seen that the battery with the ether-based electrolyte has much lower reaction resistance than those with the carbonate electrolyte. Meanwhile, the DEGDME-based electrolyte presents high sodium ion diffusion coefficients (D_{Na^+}) with an average value of 2.0×10^{-10} cm² s⁻¹ during

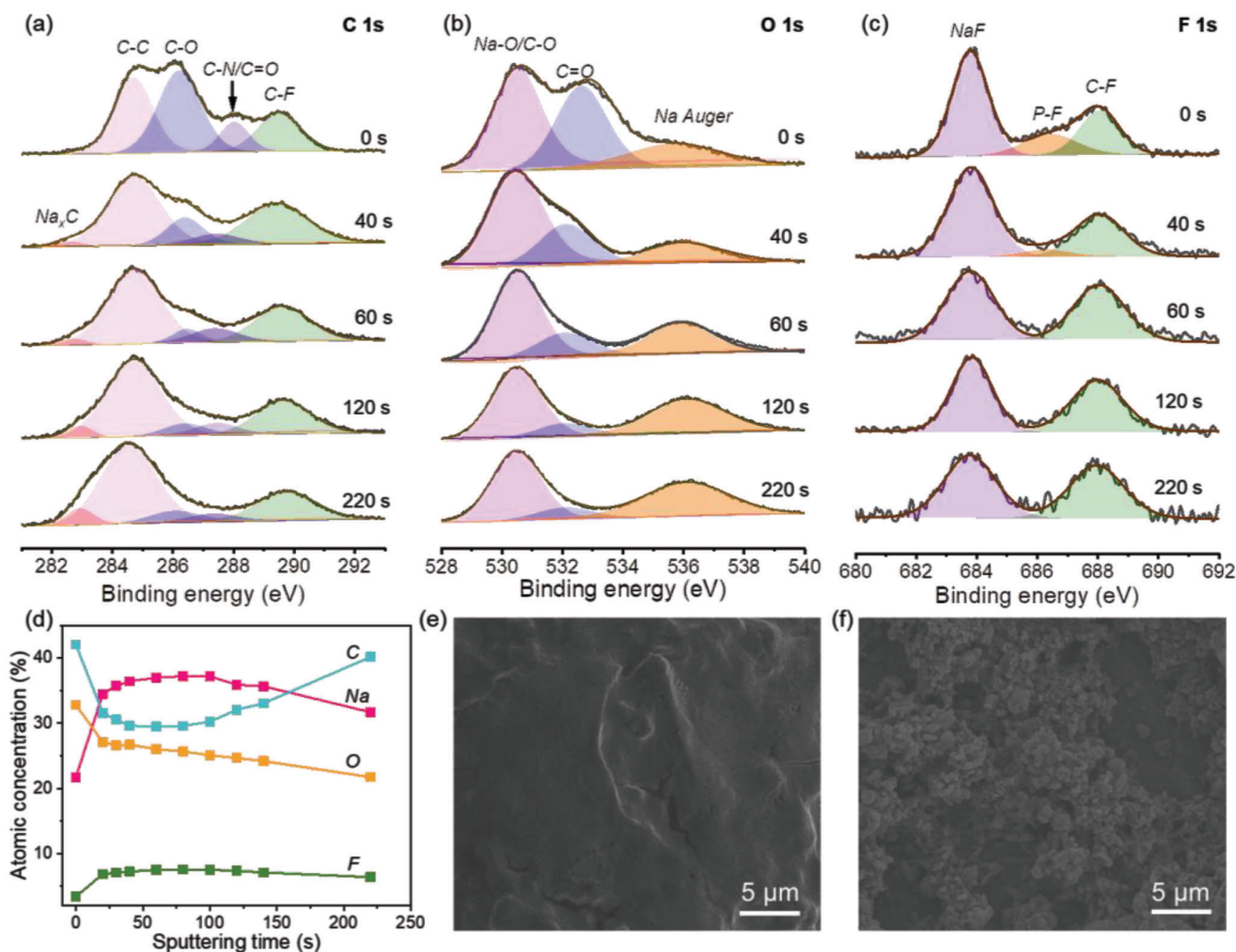


Figure 4. XPS spectra as a function of SEI depth for Sn@NC after 10 cycles at 0.1 A g^{-1} in DEGME-based electrolyte: a) C 1s, b) O 1s, c) F 1s, and d) the atomic concentrations. SEM images of the Sn@NC anodes at 1.0 A g^{-1} after 400 cycles in the e) DEGME-, and f) EC/PC-based electrolyte.

sodiation/desodiation (Figure 3f), which is five times higher than that in EC/PC-based electrolyte ($3.7 \times 10^{-11} \text{ cm}^2 \text{ s}^{-1}$).

Figure 3g shows the cycling performance of Sn@NC electrodes at 1.0 A g^{-1} in both electrolytes. The Sn@NC electrodes delivered a reversible capacity of 474 mAh g^{-1} after 400 cycles in DEGME-based electrolyte. On the contrary, the electrode only delivered a low capacity of 34.7 mAh g^{-1} in the EC/PC-based electrolyte under the same test conditions. It is worth noting that the capacity mainly stems from the Sn core, and the NC surface contributes a negligible capacity of $\approx 10 \text{ mAh g}^{-1}$ at 1.0 A g^{-1} (Figure S17, Supporting Information), which proves reversible intercalation/deintercalation of sodium ions in the NC electrode. Moreover, the CE of the batteries using ether-based electrolyte rapidly increases to $\approx 100\%$ after several cycles, while the CE with carbonate electrolyte continuously fluctuates near an average value of 97.5%. The low CE may result from the continuous fragmentation/formation of the SEI, indicating that the carbonate electrolyte is incompatible with the N-doped carbon-coated tin anode. The long cyclic performance of Sn@NC electrodes in the DEGME-based electrolyte was also evaluated at a high rate

of 5 A g^{-1} and maintained an impressive high capacity of 347 mAh g^{-1} after 10 000 cycles (Figure 3h). Moreover, the Sn@NC anodes with a higher mass loading of $\approx 3 \text{ mg cm}^{-2}$ also maintain a high capacity of 414.7 mAh g^{-1} at 5.0 A g^{-1} after 100 cycles in the ether-based electrolyte, demonstrating a huge potential for practical applications (Figure S18, Supporting Information).

In-depth XPS was employed to unravel the impact of different electrolytes on the Sn@NC electrode-electrolyte interface. The high-resolution C 1s spectrum of the cycled anode in the DEGME-based electrolyte indicates the existence of C–C, C–O, C–N/C=O, and C–F bonds (Figure 4a).^[39,40] The appearance of a C–F bond signal and the significant increase of C–O/C=O bond signals could be associated with the formation of SEI. In particular, the pronounced C–O bond can be attributed to the formation of a highly ionic conductive polyether in the SEI layer.^[41–43] The existence of C–O and C=O bonds on the surface of the cycled electrode is also verified by the corresponding O 1s spectrum in Figure 4b. Both the C–O and C=O bonds almost disappeared after 60 s etching, which demonstrates that a thin layer of conductive polyether and Na_2CO_3 formed on the cycled

electrode surface. Furthermore, The F 1s spectra in Figure 4c verify the existence of NaF, P–F, and C–F bonds. The NaF and P–F bonds correspond to inorganic fluorinated compounds in the SEI layer, which results from the decomposition of NaPF_6 . These fluorinated species contribute to the formation of a dense and robust SEI layer and thereby protect the electrode against the continuous decomposition of the electrolyte.^[22,23] The presence of the C–F bond can be ascribed to the existence of the DEGDM- PF_6^- complex, and the reaction between defective N-doped carbon surface and PF_6^- .^[39–42] Figure 4d shows the atomic concentrations derived from XPS depth profiles of the Sn@NC electrode in DEGDM-based electrolyte. After Ar etching for 100 s, the carbon content increased significantly, which can be ascribed to the contribution of the NC layer after the thinner SEI layer was etched away. The result agrees well with the emergence of Na_xC peak in the C 1s spectra after 120 s etching. According to the above analysis, we can conclude that the DEGDM-derived SEI film consists of both conductive organic polyether and robust inorganic components, leading to high CE and superior cycling performance.

In contrast, the surface of the cycled Sn@C anodes using the EC/PC-based electrolyte is dominated by unstable C=O bonds, which may mainly come from the decomposition of the carbonate electrolyte (Figure S19, Supporting Information). The fluorine characteristic peaks are also negligible on the surface, indicating that the carbonate solvents themselves are easier to decompose than the added NaPF_6 salt. Besides, the quantified atomic concentration profiles exhibit a constant element content after etching for 420 s, implying a thick SEI layer beyond the accessible measurement range. The results were further clarified by HRTEM characterizations of the cycled anode materials, where the DEGDM-derived SEI layer exhibits a more homogeneous morphology with a thinner thickness of ≈ 6.8 nm (Figure S20, Supporting Information). By contrast, the EC/PC-based derived SEI exhibits an uneven SEI layer with a variable thickness ranging from 9.7 to 25.7 nm.

The structural evolution of Sn@NC anodes upon cycling in both electrolytes was further examined by SEM and TEM (Figures S21–S26, Supporting Information). The fully sodiated Sn@NC anode in DEGDM-based electrolyte displays a compact and flat surface, and the nanorods' morphology is visible after desodiation. In contrast, a coarse surface with a few cracks was observed in the sodiated composite using the EC/PC-based electrolyte, which remains unchanged after charging. The thick layer observed on the electrodes cycled in EC/PC-based electrolyte could be attributed to the formation of unstable organic SEI film because of the continuous decomposition of carbonate solvents. The cross-section SEM images show that the electrode thickness increases after full sodiation in both systems; however, the Sn@NC in EC/PC-based electrolyte experienced a more significant volume expansion. After 50 cycles, the composite electrode in the DEGDM-based electrolyte maintained its dense structure as in the 1st cycle, whereas the electrodes in EC/PC-based electrolyte became nebulous and prone to detachment from the copper foil (Figures S21–S24, Supporting Information). This phenomenon is also verified by the top view of the cycled anodes in Figure 4e,f. The electrode surface cycled in the DEGDM-based electrolyte is smooth. However, many coarse particles and even the bare current collectors are observed in the electrodes with the EC/PC-based electrolyte. The ex situ TEM images of the fully so-

diated anode in the DEGDM-based electrolyte illustrate that the voids between the nanorods first accommodate the volume expansion of the tin nanorods, followed by a slight expansion of the whole Sn@NC flower (Figure S25a, Supporting Information). The NC surface confined the structural variation and buffered the accompanied internal stress, benefiting the structural stability of the electrode. After desodiation, the flower structure shrunk with a small fraction of voids emerging under the carbon surface. Notably, an intact outer carbon layer was witnessed, demonstrating the robustness of the NC layer (Figure S25b, Supporting Information). More importantly, the structure of the Sn@NC electrode remains intact in the DEGDM-based electrolyte after the 50th cycle, with a slight thickness increase of the NC surface (Figure S26a–c, Supporting Information). Furthermore, the lattice fringes belonging to metallic Sn were identified in the inner core, indicating the anode's excellent structural stability in the DEGDM-based electrolyte. On the contrary, the surface coating layer experienced a more significant volume expansion after the 1st cycle in the EC/PC-based electrolyte, and the N-doped carbon shell was utterly destroyed along with the collapse of the Sn nanorods after 50 cycles (Figure S26d–f, Supporting Information). It can be ascribed to the larger Na^+ solvation shell in the carbonate electrolyte (discussed in the later simulation section) and the co-intercalation of solvated cations that cause the structural degradation of both the carbon surface and the internal Sn.

The variation of the electrode structure could influence the impedance of the battery cells. We measured electrochemical impedance spectroscopy (EIS) of Sn@NC electrodes in both electrolytes at different cycles (Figure S27, Supporting Information).^[44] The charge transfer resistance increases slightly in the first 100 cycles and stays almost constant from 100 to 400 cycles, which could be assigned to the intact and robust SEI, as well as the excellent structural stability of the Sn@NC in the DEGDM-based electrolyte. However, in the EC/PC-based electrolyte the charge transfer resistance and Warburg impedance continuously rise during 400 discharge/charge cycles due to the degradation of both the carbonate electrolyte and electrode (Figure S28, Supporting Information). Based on the above analyses, we can conclude that the ether-based electrolyte with favorable Na^+ reaction kinetics and good chemical stability is more compatible with the N-doped carbon surface-modified tin anode. Furthermore, the formation of a stable organic-inorganic hybrid SEI film in the ether-based electrolyte protects the alloy anode and leads to excellent long cyclic performance.

The performance of the Sn@NC anodes was further evaluated in full cells coupling with $\text{Na}_3\text{V}_2(\text{PO}_4)_3/\text{carbon}$ (NVP/C) cathodes in a wide temperature range of -20 , 0 , 25 , and 50 °C (Figure 5a). The NVP/C material was prepared via a solid-state method based on the previous report (Figure S29, Supporting Information).^[45,46] The sodium storage performance of the NVP/C cathodes was first investigated in a half cell using sodium metal as counter electrodes. The NVP/C cathode shows a typical flat charge/discharge plateau at about 3.4 V and a retained capacity of 99.7 mAh g^{-1} at 1.0 A g^{-1} after 100 cycles (Figure S30, Supporting Information).^[47–49] The full batteries were assembled with NVP/C cathode, Sn@NC anode (active mass ratio of cathode and anode is 5:1), and DEGDM-based electrolyte.

Figure 5b shows the charge/discharge curves of the full cell at 0.1 A g^{-1} under different temperatures. The Sn@NC || NVP/C

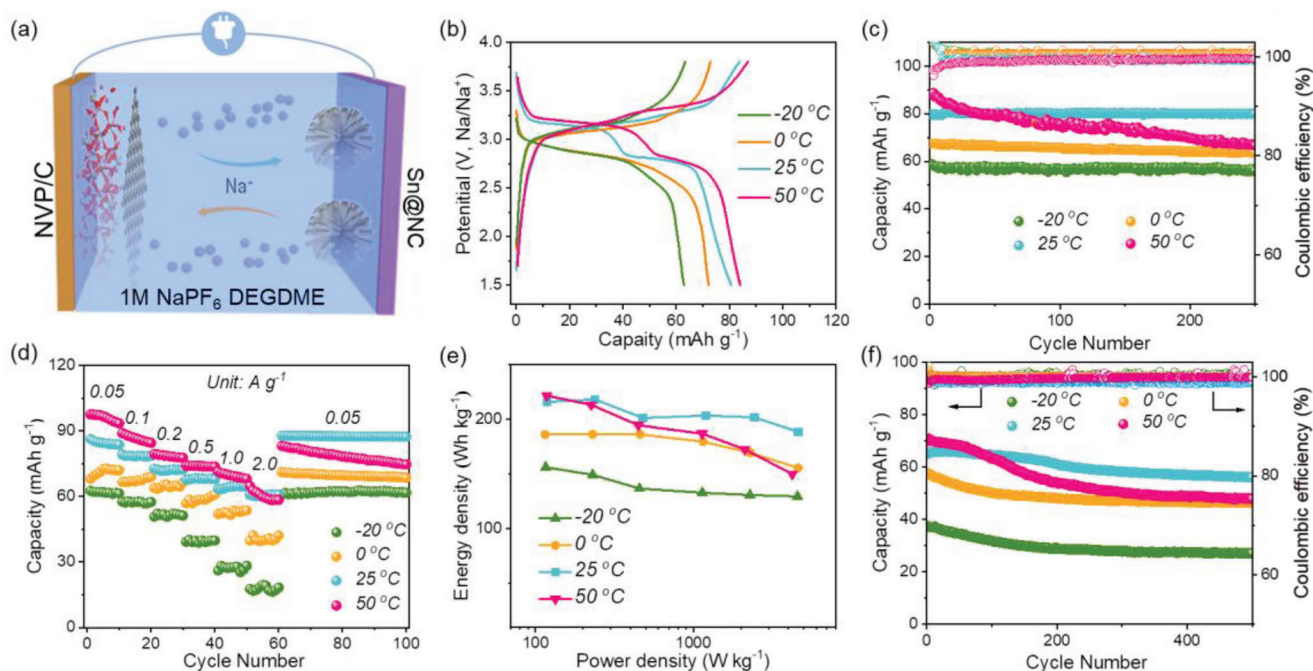


Figure 5. a) Schematic configuration, b) discharge/charge profiles, and c) cycling performance of a typical Sn@NC||NVP/C full SIB at 0.1 A g^{-1} at different temperatures. d) Rate performance, e) Ragone plot, and f) long cycling performance at 1 A g^{-1} of the Sn@NC||NVP/C full SIB at temperatures of -20 , 0 , 25 , and $50 \text{ }^\circ\text{C}$.

full cell delivered a reversible capacity of 80.7 mAh g^{-1} at $25 \text{ }^\circ\text{C}$ (the capacity is calculated based on the total mass of anode and cathode active materials), and the capacity is maintained at nearly 80% even at a low temperature of $-20 \text{ }^\circ\text{C}$. The Sn@N||NVP/C full SIBs showed steady cycling performance over 250 cycles at -20 , 0 , and $25 \text{ }^\circ\text{C}$ (Figure 5c). Although a slightly faster capacity decay was observed at $50 \text{ }^\circ\text{C}$, which might be ascribed to the more severe electrolyte side reactions at the elevated temperature, the cell still achieved a capacity of 66.6 mAh g^{-1} at 0.1 mA g^{-1} after 250 cycles. Additionally, the full SIBs exhibit superior rate performance at different temperatures. A capacity of 60.7 mAh g^{-1} (at $25 \text{ }^\circ\text{C}$) and 40.3 mAh g^{-1} (at $0 \text{ }^\circ\text{C}$) can be achieved at a high current density of 2 A g^{-1} (Figure 5d). Figure S31, Supporting Information presents the charge/discharge curves of the full cell at different current densities and different temperatures, which are used to obtain the Ragone plot. As shown in Figure 5e, the Sn@NC||NVP/C full SIBs exhibit a high energy density of 215 Wh kg^{-1} at a power density of 118 W kg^{-1} at room temperature. Even at a high power of 4608 W kg^{-1} , the full SIB also shows a high energy density of 187 Wh kg^{-1} . The performance does not experience an obvious decay at low or high temperatures. Besides, the Sn@NC||NVP/C full SIBs also exhibited excellent long-cyclic performance across the wide temperature range, implying a high potential for practical application in a diversity of future markets (Figure 5f).

We employed DFT calculations to fundamentally understand the different behavior of the two electrolytes. First, we calculated the highest occupied molecular orbital (HOMO) and lowest unoccupied molecular orbital (LUMO) energy levels of various solvents used in this work. The DEGDM shows a larger energy level difference for electron transport from HOMO to LUMO

than that of EC and PC (Figure 6a), indicating its better stability and resistance to decomposition. Therefore, in the DEGDM-based electrolyte, NaPF₆ preferred to decompose and be involved in forming a fluorinated SEI film. In contrast, the EC and PC are prone to decompose first and form an SEI mainly consisting of unstable C=O compounds. Moreover, the DEGDM solvent and the [NaPF₆-DEGDM]⁺ complex both show higher HOMO energy (Figure S32, Supporting Information), indicating that the DEGDM-based electrolyte is easier to donate electrons to facilitate the formation of cathode electrolyte interphase (CEI)^[42,50]. Therefore, the DEGDM-based electrolyte can function well for both anode and cathode and thereby improve the electrochemical performance of the full cells.

The solvation structure of Na⁺ is crucial to electrochemical performance as Na⁺ ions need to first intercalate into the N-doped carbon surface and then react with metallic Sn. Therefore, we investigated the solvation structures of Na⁺ ions in both electrolytes by Ab initio molecular dynamic (AIMD) simulations (Figure 6b and Figure S33, Supporting Information). Radial distribution functions (RDFs) of Na-O and Na-F pairs in both electrolytes are shown in Figure 6c. Compared to the Na-F_{EC/PC} pair, the more prominent *g*(*r*) in the Na-F_{DEGDM} pair indicates a stronger Na-F interaction between PF₆⁻ and Na⁺ in the DEGDM-based electrolyte. It facilitates the decomposition of PF₆⁻ rather than the DEGDM solvent and contributes to the formation of dense fluorine-rich SEI on the electrode surface.^[51] Meanwhile, the Na-O_{DEGDM} pair only shows a sharp peak of around 1.91 \AA , indicating that DEGDM only distributes in the first solvation shell.^[52,53] In contrast, two distinct peaks are presented in the Na-O_{PC/EC} pair, indicating that more carbonate molecules coordinate with Na⁺ to reach a stable double-shell solvation structure.

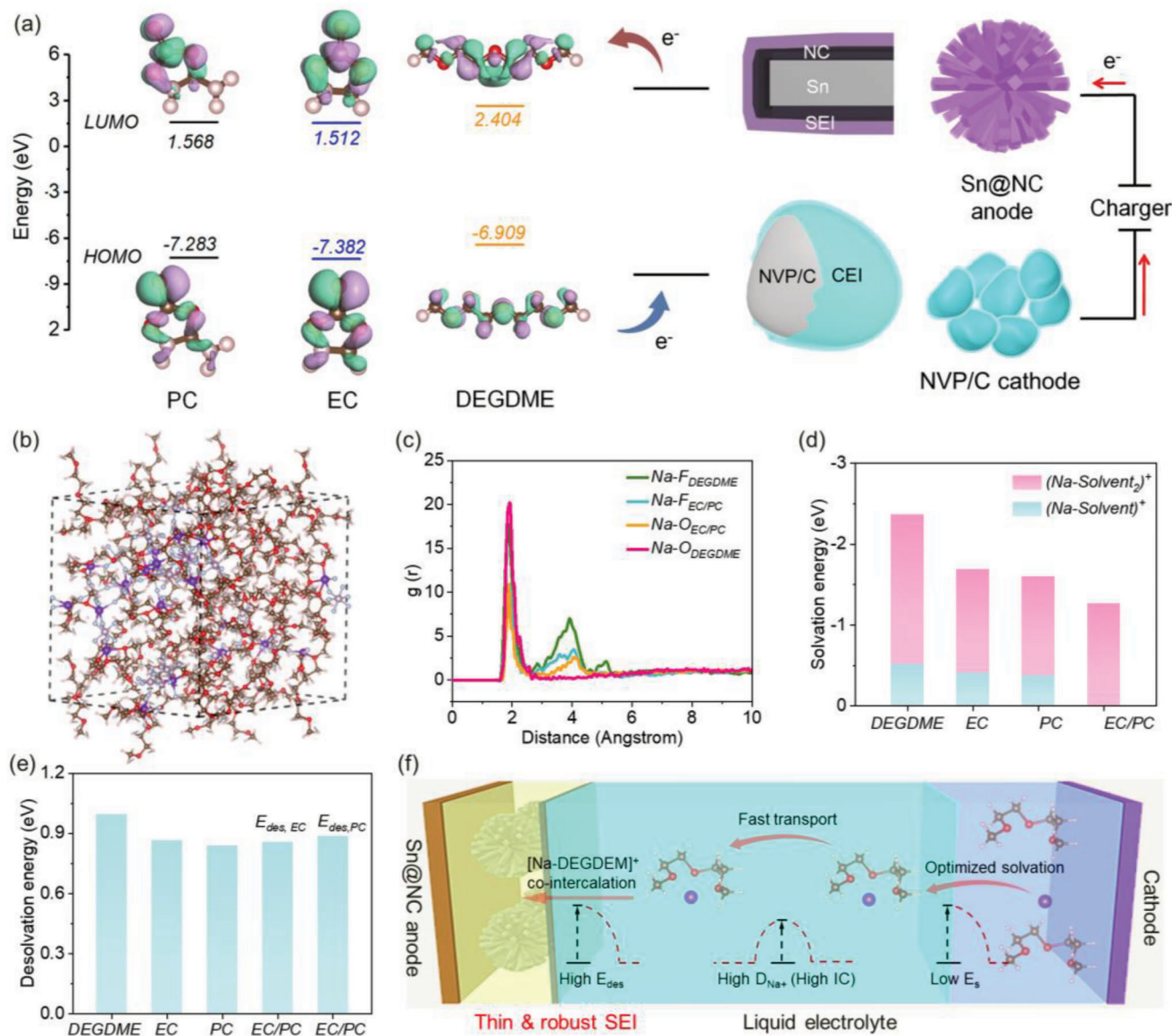


Figure 6. a) Diagram of the HOMO and LUMO energy levels showing the electron acceptance and donation ability of EC, PC, and DEGME. b) AIMD simulation snapshots of the DEGME-based electrolyte. c) Radial distribution functions $g(r)$ of Na-O and Na-F pairs in both electrolytes. d) Solvation energy and e) desolvation energy of Na⁺-solvent complexes. f) Schematic illustration of reaction kinetics of Sn@NC full cells with DEGME-based electrolyte.

Compared to the carbonate-based electrolyte, the smaller Na⁺ solvation shell of the DEGME-based electrolyte leads to a weaker steric repulsion at the interface and faster reaction kinetics.

To better unravel the chemical reactions at the solid-electrolyte interface, we further calculated the specific solvation energy (E_s) and desolvation energy ($E_{des,x}$) of all the [Na-solvent_x]⁺ complexes relating to this work (Figure S34, Supporting Information). The calculated E_s values of [Na-DEGDM]⁺, [Na-DEGDM₂]⁺, [Na-EC]⁺, [Na-EC₂]⁺, [Na-PC]⁺, [Na-PC₂]⁺, and [Na-EC/PC]⁺, are -0.51, -1.85, -0.41, -1.28, -0.38, -1.22, and -1.27 eV, respectively (Figure 6d). Therefore, the carbonate solvation sheath is more prone to accept electrons and decompose due to the weak solvation energy. However, the DEGME is firmly solvated

with Na⁺ in the ether-based electrolyte, which isolates PF₆⁻ anions and enables them to preferentially decompose and form a fluorine-rich inorganic SEI inner layer.^[54–56] Moreover, the desolvation process at the interface between electrodes and electrolytes would affect the electrochemical reaction process. The [Na-DEGDM]⁺ complexes also exhibit a higher desolvation energy compared to the other [Na-solvent_x]⁺ complexes (Figure 6e and Figure S35, Supporting Information), indicating that the [Na-DEGDM]⁺ complexes more easily co-intercalate into the NC layer, which will be favorable for superior rate capability and cycling performance.^[57–59]

Figure 6f illustrates the overall effects and reaction mechanism of the surface- and interface-engineered sodium-ion

batteries. The Na^+ ions in the ether-based electrolyte are strongly solvated with DEGDME molecules. Meanwhile, the DEGDME with high LUMO and low HOMO is not only resistant to decomposition, which enables the PF_6^- anions to participate in the formation of the robust inorganic inner SEI but also contributes to the formation of a thin layer of ionic-conductive polyether SEI outer layer. More importantly, the single-shelled $[\text{Na-DEGDME}_x]^+$ complexes with fast mobility can pass through the N-doped layer to react with active tin materials, leading to excellent rate performance at wide temperature ranges. Last but not least, the surface modification and the stable interface synergistically confine the volume change of the tin alloy anode and benefit long cycling performance.

3. Conclusion

In summary, we combined surface and interface engineering strategies to achieve high-performance alloy anodes for sodium-ion batteries. Theoretical calculations and experimental results coherently demonstrated that the nitrogen-doped carbon surface coating functions well with the DEGDME-based electrolyte modulated interface, resulting in remarkably improved sodium reaction kinetics and electrode structural stability. Additionally, the DEGDME with better stability and stronger sodium solvation energy can promote the formation of a stable SEI consisting of NaPF_6 decomposed by the fluorine-rich inner layer and DEGDME-derived highly ionic-conductive polyether outer layer. The robust SEI effectively stabilizes the electrodes and inhibits the decomposition of the electrolyte. Therefore, $\text{Sn@NC} \parallel \text{NVP/C}$ full SIB exhibited high power density (4608 W kg^{-1}) and energy density (187 Wh kg^{-1}) as well as excellent cycling stability in a wide temperature range from -20 to 50°C . This work validates the surface and interface engineering approach for improving the performance of alloy-based materials for sodium storage, and it is expected to advance the development of high-energy all-climate energy storage devices.

Supporting Information

Supporting Information is available from the Wiley Online Library or from the author.

Acknowledgements

C.W. appreciates the Priority Academic Program Development of Jiangsu Higher Education Institutions and the Postgraduate Research & Practice Innovation Program of Jiangsu Province (grant number KYCX21_3197). X.G. and G.W. acknowledge the financial support by the Australian Research Council (ARC) through the ARC Discovery Projects (DP200101249, DP210101389) and ARC Research Hub for Integrated Energy Storage Solutions (IH180100020).

Open access publishing facilitated by University of Technology Sydney, as part of the Wiley - University of Technology Sydney agreement via the Council of Australian University Librarians.

Conflict of Interest

The authors declare no conflict of interest.

Data Availability Statement

The data that support the findings of this study are available from the corresponding author upon reasonable request.

Keywords

sodium-ion batteries, solid-electrolyte interfaces, solvation effect, surface engineering, tin, wide-temperature applications

Received: February 2, 2023

Revised: May 21, 2023

Published online: June 22, 2023

- [1] S. F. Liu, X. Ji, J. Yue, S. Y. Hou, P. F. Wang, C. Y. Cui, J. Chen, B. Shao, J. R. Li, F. D. Han, J. P. Tu, C. S. Wang, *J. Am. Chem. Soc.* **2020**, *142*, 2438.
- [2] J. Chen, X. L. Fan, Q. Li, H. B. Yang, M. R. Khoshi, Y. B. Xu, S. Hwang, L. Chen, X. Ji, C. Y. Yang, H. X. He, C. M. Wang, E. Garfunkel, D. Su, O. Borodin, C. S. Wang, *Nat. Energy* **2020**, *5*, 386.
- [3] A. Ponrouch, E. Marchante, M. Courty, J. M. Tarascon, M. R. Palacin, *Energy Environ. Sci.* **2012**, *5*, 8572.
- [4] C. X. Chu, R. Li, F. P. Cai, Z. C. Bai, Y. X. Wang, X. Xu, N. N. Wang, J. Yang, S. X. Dou, *Energy Environ. Sci.* **2021**, *14*, 4318.
- [5] K. X. Lei, F. J. Li, C. N. Mu, J. B. Wang, Q. Zhao, C. C. Chen, J. Chen, *Energy Environ. Sci.* **2017**, *10*, 552.
- [6] W. Luo, F. Shen, C. Bommier, H. L. Zhu, X. L. Ji, L. B. Hu, *Acc. Chem. Res.* **2016**, *49*, 231.
- [7] H. S. Li, L. L. Peng, Y. Zhu, D. H. Chen, X. G. Zhang, G. H. Yu, *Energy Environ. Sci.* **2016**, *9*, 3399.
- [8] S. Q. Zhao, Z. Q. Guo, J. Yang, C. Y. Wang, B. Sun, G. X. Wang, *Small* **2021**, *17*, 2007431.
- [9] C. C. Wang, D. F. Du, M. M. Song, Y. H. Wang, F. J. Li, *Adv. Energy Mater.* **2019**, *9*, 1900022.
- [10] X. D. Lin, G. D. Zhou, J. P. Liu, J. Yu, M. B. Effat, J. X. Wu, F. Ciucci, *Adv. Energy Mater.* **2020**, *10*, 2001235.
- [11] Q. Li, K. Z. Jiang, X. Li, Y. Qiao, X. Y. Zhang, P. He, S. H. Guo, H. S. Zhou, *Adv. Energy Mater.* **2018**, *8*, 1801162.
- [12] J. Yang, J. B. Li, T. Y. Wang, P. H. L. Notten, H. Ma, Z. G. Liu, C. Y. Wang, G. X. Wang, *Chem. Eng. J.* **2021**, *407*, 127169.
- [13] J. Yang, W. Z. Bao, P. Jaumaux, S. T. Zhang, C. Y. Wang, G. X. Wang, *Adv. Mater. Interfaces* **2019**, *6*, 1802004.
- [14] M. M. Lao, Y. Zhang, W. B. Luo, Q. Y. Yan, W. P. Sun, S. X. Dou, *Adv. Mater.* **2017**, *29*, 1700622.
- [15] M. Bai, Y. Liu, K. Zhang, X. Tang, S. Liu, Y. Ma, *Energy Storage Mater.* **2021**, *38*, 499.
- [16] Z. Li, J. Ding, D. Mitlin, *Acc. Chem. Res.* **2015**, *48*, 1657.
- [17] T. Palaniselvam, M. Goktas, B. Anothumakkool, Y. N. Sun, R. Schmuck, L. Zhao, B. H. Han, M. Winter, P. Adelhelm, *Adv. Funct. Mater.* **2019**, *29*, 1900790.
- [18] B. Zhang, G. Rousse, D. Foix, R. Dugas, D. A. Corte, J. M. Tarascon, *Adv. Mater.* **2016**, *28*, 9824.
- [19] Y. H. Xu, Y. J. Zhu, Y. H. Liu, C. S. Wang, *Adv. Energy Mater.* **2013**, *3*, 128.
- [20] Z. Q. Lv, T. Y. Li, X. Hou, C. P. Wang, H. M. Zhang, J. W. Yan, Q. Zheng, X. F. Li, *Chem. Eng. J.* **2022**, *430*, 133143.
- [21] J. Zhang, D. W. Wang, W. Lv, L. Qin, S. Z. Niu, S. W. Zhang, T. F. Cao, F. Y. Kang, Q. H. Yang, *Adv. Energy Mater.* **2018**, *8*, 1801361.
- [22] H. C. Yuan, F. X. Ma, X. B. Wei, J. L. Lan, Y. Liu, Y. H. Yu, X. P. Yang, H. S. Park, *Adv. Energy Mater.* **2020**, *10*, 2001418.

- [23] B. S. Qin, A. Schiele, Z. Jusys, A. Mariani, T. Diemant, X. Liu, T. Brezesinski, R. J. Behm, A. Varzi, S. Passerini, *ACS Appl. Mater. Interfaces* **2020**, *12*, 3697.
- [24] D. M. C. Ould, S. Menkin, C. A. O'Keefe, F. Coowar, J. Barker, C. P. Grey, D. S. Wright, *Angew. Chem., Int. Ed.* **2021**, *60*, 24882.
- [25] P. Barnes, K. Smith, R. Parrish, C. Jones, P. Skinner, E. Storch, Q. White, C. Deng, D. Karsann, M. L. Lau, J. J. Dumais, E. J. Dufek, H. Xiong, *J. Power Sources* **2020**, *447*, 227363.
- [26] J. Pan, S. L. Chen, D. P. Zhang, X. N. Xu, Y. W. Sun, F. Tian, P. Gao, J. Yang, *Adv. Funct. Mater.* **2018**, *28*, 1804672.
- [27] Z. Y. Wang, K. Z. Dong, D. Wang, F. Chen, S. H. Luo, Y. G. Liu, C. N. He, C. S. Shi, N. Q. Zhao, *Chem. Eng. J.* **2019**, *371*, 356.
- [28] Y. Y. Li, C. Z. Ou, J. L. Zhu, Z. G. Liu, J. L. Yu, W. W. Li, H. Y. Zhang, Q. B. Zhang, Z. P. Guo, *Nano Lett.* **2020**, *20*, 2034.
- [29] Y. T. Bie, J. Yang, X. L. Liu, J. L. Wang, Y. N. Nuli, W. Lu, *ACS Appl. Mater. Interfaces* **2016**, *8*, 2899.
- [30] D. T. Zhao, Z. R. Xu, J. P. Chada, C. A. Carrero, D. C. Rosenfeld, J. L. Rogers, I. Hermans, G. W. Huber, *ACS Catal.* **2017**, *7*, 7479.
- [31] K. C. Wasalathilake, S. N. S. Hapuarachchi, Y. Zhao, J. F. S. Fernando, H. Chen, J. Y. Nerkar, D. Golberg, S. Zhang, C. Yan, *ACS Appl. Energy Mater.* **2019**, *3*, 521.
- [32] C. Y. Cui, J. T. Xu, Y. Q. Zhang, Z. X. Wei, M. X. Mao, X. Lian, S. Y. Wang, C. Y. Yang, X. L. Fan, J. M. Ma, C. S. Wang, *Nano Lett.* **2018**, *19*, 538.
- [33] Q. F. Zhang, Y. Cui, E. Wang, *Modell. Simul. Mater. Sci. Eng.* **2013**, *21*, 074001.
- [34] S. Y. Sayed, W. P. Kalisvaart, E. J. Lubber, B. C. Olsen, J. M. Buriak, *ACS Appl. Energy Mater.* **2020**, *3*, 9950.
- [35] T. Li, U. Gulzar, R. Proietti Zaccaria, C. Capiglia, S. A. Hackney, K. E. Aifantis, *J. Phys. Chem. C* **2019**, *123*, 15244.
- [36] Y. S. Zhu, Z. Qian, J. Song, W. Z. Du, J. Pan, D. D. Wang, J. Yang, *Nano Lett.* **2021**, *21*, 3588.
- [37] D. W. Su, S. X. Dou, G. X. Wang, *Nano Energy* **2015**, *12*, 88.
- [38] C. C. Wang, L. B. Wang, F. J. Li, F. Y. Cheng, J. Chen, *Adv. Mater.* **2017**, *29*, 1702212.
- [39] M. Y. Ma, H. R. Cai, C. L. Xu, R. Z. Huang, S. R. Wang, H. L. Pan, Y. S. Hu, *Adv. Funct. Mater.* **2021**, *31*, 2100278.
- [40] J. Yang, T. Y. Wang, X. Guo, X. X. Sheng, J. B. Li, C. Y. Wang, G. X. Wang, *Nano Res.* **2021**, *16*, 5592.
- [41] Y. Q. Wang, P. X. Bai, B. F. Li, C. Zhao, Z. F. Chen, M. J. Li, H. Su, J. X. Yang, Y. H. Xu, *Adv. Energy Mater.* **2021**, *11*, 2101972.
- [42] J. Zhang, D. W. Wang, W. Lv, S. Zhang, Q. H. Liang, D. Q. Zheng, F. Y. Kang, Q. H. Yang, *Energy Environ. Sci.* **2017**, *10*, 370.
- [43] J. Q. Huang, X. Y. Guo, X. Q. Du, X. Y. Lin, J. Q. Huang, H. Tan, Y. Zhu, B. Zhang, *Energy Environ. Sci.* **2019**, *12*, 1550.
- [44] K. Westman, R. Dugas, P. Jankowski, W. Wieczorek, G. Gachot, M. Morcrette, E. Irisarri, A. Ponrouch, M. R. Palacín, J. M. Tarascon, P. Johansson, *ACS Appl. Energy Mater.* **2018**, *1*, 2671.
- [45] S. Li, Y. F. Dong, L. Xu, X. Xu, L. He, L. Q. Mai, *Adv. Mater.* **2014**, *26*, 3545.
- [46] J. L. Xu, J. Z. Chen, S. Zhou, C. P. Han, M. J. Xu, N. Zhao, C. P. Wong, *Nano Energy* **2018**, *50*, 323.
- [47] Z. Yang, G. L. Li, J. Y. Sun, L. X. Xie, Y. Jiang, Y. H. Huang, S. Chen, *Energy Storage Mater.* **2020**, *25*, 724.
- [48] H. Ma, T. Y. Wang, J. B. Li, J. Yang, Z. G. Liu, N. Wang, D. W. Su, C. Y. Wang, *Chem. Asian J.* **2021**, *16*, 2314.
- [49] X. M. Li, S. J. Wang, X. Tang, R. Zang, P. Li, P. X. Li, Z. M. Man, C. Li, S. S. Liu, Y. H. Wu, G. X. Wang, *J. Colloid Interface Sci.* **2019**, *539*, 168.
- [50] J. G. Han, J. B. Lee, A. Cha, T. K. Lee, W. Cho, S. Chae, S. J. Kang, S. K. Kwak, J. Cho, S. Y. Hong, N. S. Choi, *Energy Environ. Sci.* **2018**, *11*, 1552.
- [51] X. Q. Zhang, X. Chen, L. P. Hou, B. Q. Li, X. B. Cheng, J. Q. Huang, Q. Zhang, *ACS Energy Lett.* **2019**, *4*, 411.
- [52] X. D. Ren, S. R. Chen, H. Lee, D. H. Mei, M. H. Engelhard, S. D. Burton, W. G. Zhao, J. M. Zheng, Q. Y. Li, M. S. Ding, M. Schroeder, J. Alvarado, K. Xu, Y. S. Meng, J. Liu, J. G. Zhang, W. Xu, *Chem* **2018**, *4*, 1877.
- [53] Z. Tian, Y. Zou, G. Liu, Y. Wang, J. Yin, J. Ming, H. N. Alshareef, *Adv. Sci.* **2022**, *9*, 2201207.
- [54] L. Li, L. Liu, Z. Hu, Y. Lu, Q. Liu, S. Jin, Q. Zhang, S. Zhao, S. L. Chou, *Angew Chem Int Ed Engl* **2020**, *59*, 12917.
- [55] H. Kim, K. Lim, G. Yoon, J. H. Park, K. Ku, H. D. Lim, Y. E. Sung, K. Kang, *Adv. Energy Mater.* **2017**, *7*, 1700418.
- [56] W. Cai, Y. X. Yao, G. L. Zhu, C. Yan, L. L. Jiang, C. He, J. Q. Huang, Q. Zhang, *Chem. Soc. Rev.* **2020**, *49*, 3806.
- [57] H. R. Cheng, Q. J. Sun, L. L. Li, Y. G. Zou, Y. Q. Wang, T. Cai, F. Zhao, G. Liu, Z. Ma, W. Wahyudi, Q. Li, J. Ming, *ACS Energy Lett.* **2022**, *7*, 490.
- [58] T. Sun, X. L. Feng, Q. Q. Sun, Y. Yu, G. B. Yuan, Q. Xiong, D. P. Liu, X. B. Zhang, Y. Zhang, *Angew. Chem., Int. Ed.* **2021**, *60*, 26806.
- [59] J. Y. Yang, J. F. Ruan, Q. Li, F. Fang, Y. Song, D. L. Sun, F. Wang, *Adv. Funct. Mater.* **2022**, *32*, 2200566.